Computational hardness of spin-glass problems with tile-planted solutions

Dilina Perera,[1, *] Firas Hamze,[2] Jack Raymond,[2] Martin Weigel,[3] and Helmut G. Katzgraber[4, 1, 5]

[1]*Department of Physics and Astronomy, Texas A&M University, College Station, Texas 77843-4242, USA*
[2]*D-Wave Systems, Inc., 3033 Beta Avenue, Burnaby, British Columbia, Canada V5G 4M9*
[3]*Applied Mathematics Research Centre, Coventry University, Coventry CV1 5FB, England*
[4]*Microsoft Quantum, Microsoft, Redmond, Washington 98052, USA*
[5]*Santa Fe Institute, 1399 Hyde Park Road, Santa Fe, New Mexico 87501, USA*

We investigate the computational hardness of spin-glass instances on a square lattice, generated via a recently introduced tunable and scalable approach for planting solutions. The method relies on partitioning the problem graph into edge-disjoint subgraphs, and planting frustrated, elementary subproblems that share a common local ground state, which guarantees that the ground state of the entire problem is known a priori. Using population annealing Monte Carlo, we compare the typical hardness of problem classes over a large region of the multi-dimensional tuning parameter space. Our results show that the problems have a wide range of tunable hardness. Moreover, we observe multiple transitions in the hardness phase space, which we further corroborate using simulated annealing and simulated quantum annealing. By investigating thermodynamic properties of these planted systems, we demonstrate that the harder samples undergo magnetic ordering transitions which are also ultimately responsible for the observed hardness transitions on changing the sample composition.

I. INTRODUCTION

Optimization problems with many minima occur in a multitude of fields, including finance, engineering, materials sciences, and machine learning. While a range of problems such as shortest path, maximum flow and minimum spanning tree can be elegantly solved with algorithms of a run time growing polynomially with the system size [1], many of the most interesting problems are known to be NP hard, and, as a consequence, polynomial-time algorithms are very unlikely to exist. Among discrete optimization problems many systems can be mapped onto the Ising spin glass [2, 3] as a central object of study in statistical physics. Its features of frustration and random disorder that are believed to be fundamental to the existence of a spin-glass phase [4] lead to the multitude of local minima separated by barriers — the complex (free) energy landscape — that are also at the heart of hard optimization problems more generally [3, 5]. Besides the overlap in model systems, statistical physics methods have also proven particularly valuable in elucidating the structure of the solution space of optimization problems [6] and the occurrence of phase transitions in sample hardness as suitable control parameters are tuned [7]. Moreover, many heuristic techniques for optimization such as simulated annealing [8], parallel tempering Monte Carlo [9–13], population annealing Monte Carlo [14–17], and simulated quantum annealing using quantum Monte Carlo [18–21], have been derived from concepts in statistical and quantum physics.

Recent years have witnessed the advent of special-purpose devices for discrete optimization. Most noteworthy are the commercially-available analog D-Wave quantum annealing devices [22, 23], which strive to minimize Ising Hamiltonians by exploiting quantum tunneling and superposition. The latest machine, the D-Wave 2000Q, allows for the optimization of instances with up to 2000 Ising variables, although sparse connectivity of the native graph and the noise due to control errors [24–26] pose limitations for practical applications. As of now, no experimental evidence of a quantum advantage for generic optimization applications has been discovered, while there are some early indications of a quantum advantage when using the machine as a physical simulator. However, a number of recent studies have shown a speedup for the device over selected classical algorithms for specific classes of synthetic problems [27, 28]. In addition to D-Wave devices, a number of further experimental hardware-based solvers have been introduced, for example, the Coherent Ising machine (optical) [29, 30], and the CMOS-based Fujitsu Digital Annealer [31, 32] studied recently by Aramon *et al*. [33].

With the ensuing recent growth in interest in hardware- and software-based Ising solvers, there is an increasing demand for hard tunable benchmark problems for performance comparisons [34]. Synthetic benchmark problems whose ground states are known *a priori* by construction, commonly known as samples with *planted solutions* [35], are particularly advantageous in this regard. Ideally, the hardness of such problems should be readily tunable, and the construction procedure should be scalable to larger system sizes with reasonable computational effort. A number of solution planting schemes have been proposed for the case of short-range Ising spin-glasses. For example, reference [36] presented an approach in which constraint satisfaction problems in the form of cycles of couplers (i.e., frustrated loops) are embedded into an arbitrary graph. Although the problem hardness is tunable, the range of coupler strength is uncontrolled and increases with the system size, which leads to amplified control errors in analog devices with finite precision such as the D-Wave machines. Reference [37] introduced a variation of the method with limited range of coupling strength that mitigates the precision limitations. However, both methods produce problems that are easier than other standard benchmarks for a wide range of software and hardware-based solvers [38].

Reference [39] proposed an adaptive algorithm for generating hard problems by iteratively updating the coupler values based on the time-to-solution of a chosen solver. The

*dilinanp@tamu.edu

computational resources required by the procedure, however, severely restrict the feasible size of the problems. Moreover, the method relies on the assumption that the problem hardness as predicted by the chosen solver may also extend to other solvers. In the "patch planting" method introduced in Ref. [40], the problem graphs are constructed by stitching together smaller subgraphs via couplers that ensure consistency among boundary spins. Although the method allows for the construction of arbitrarily large problems with no restrictions on coupler values or the graph topology, the resultant problems are less difficult than entirely random problems of comparable size. In addition, as the ground states of the constituent subgraphs are needed to be determined in advance, the problem construction may require considerable computational effort depending on the size and connectivity of the subgraphs.

Recently, some of the present authors proposed a planted solutions scheme [41] that circumvents several weaknesses of the aforementioned methods. Henceforth, let us refer to this approach as "tile planting." The method is based on decomposing the underlying problem graph into edge-disjoint subgraphs, and embedding a selected set of subproblems in the resulting subgraphs. The subproblems are chosen such that they share a common (local) ground state, which ensures that the ground state of the entire problem is known *a priori*. Due to the myriad ways in which subproblems can be chosen, one can construct problems with a wide range of computational complexities. The problem construction demands very low computational effort, and facilitates the generation of arbitrarily large problems on the underlying topology.

For completeness, we mention two alternate planting approaches [42, 43] that start from a set of linear equations and then use these to plant a solution for a quadratic Ising system. In particular, the Wishart planted ensemble [42] is amenable to theoretical exploration, thus allowing one to make analytical predictions for the typical computational hardness of the planted problems with a given bit precision. While this is a huge bonus, the drawback is that the planted ensemble requires a complete graph and is thus not best suited to benchmark current quantum annealing hardware where an all-to-all connectivity is extremely hard to build [23]. However, the ensemble is ideal for the benchmarking of (classical) digital annealer hardware [31, 32], as well as optical systems [29, 30].

In the present paper, we explore the computational hardness of planted problems on square lattices constructed using tile planting. By focusing on the square lattice we are able to exhaustively investigate a large region of the tuning parameter phase space, a task that is impractical for cubic lattices due to the comparatively larger phase space. Although the planarity of the underlying graph renders them exactly solvable in polynomial time using planar graph solvers [44–47], the free-energy landscape generally remains challenging for the majority of practical heuristic optimization methods that are agnostic to this special graph structure, and the resulting class of problems has many common features with non-planar variants of the tile-planting approach [41] in, e.g., three space dimensions or nonplanar graphs. It should also be noted that one can break planar methods by superficial modifications such as adding fields, but the purpose here is not to obfuscate our re-
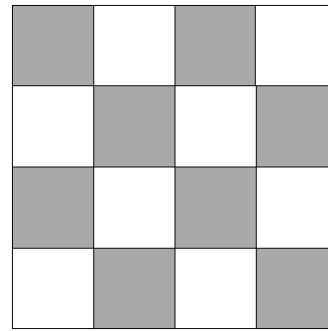

FIG. 1: Decomposition of the square lattice graph into vertex-sharing, unit cell subgraphs (shaded cells). Note that subgraphs do not share any edges. When periodic boundary conditions are imposed, each vertex is shared by exactly two subgraphs. Unit cell Ising subproblems with a common local ground state are planted on the subgraphs. The entire problem has a ground state (i.e., the planted solution) comprised of the same local ground state occupying all subgraphs.

sults through such changes.

The remainder of this paper is organized as follows. In Sec. II we outline our planted solutions scheme for square lattices, and discuss the relationship of the constructed problems to constraint satisfaction problems. In Sec. III we investigate the variations in problem difficulty across different instance classes via the population annealing Monte Carlo method. Particular emphasis is given to two specific regions in the parameter space where hardness transitions are observed, which we further investigate using simulated annealing and simulated quantum annealing. Furthermore, we investigate the thermodynamic properties of a selected set of instance classes and discuss the connection between hardness and phase behavior. Section IV presents our concluding remarks.

II.   TILE PLANTING

We start by describing our planting scheme for square lattices, which will be the focus of this paper. For a demonstration of the method for cubic lattices see Ref. [41]. Note that the approach is adaptable to arbitrary graphs, with a carefully chosen set of subproblem classes suitable for the underlying topology.

Let us consider a square lattice of linear size L with periodic boundary conditions. We denote the underlying graph as $G = (V, E)$, with vertex set V and edge set E. As illustrated in Fig. 1, by partitioning the lattice into a checkerboard pattern, we decompose the graph G into a set of vertex-sharing, unit cell subgraphs (represented by shaded cells). Note that the subgraphs do not share any edges, and with periodic boundary conditions, each vertex in V appears exactly in two subgraphs. Let C denote the vertices of a given unit cell subgraph, and $\mathcal{C}$ represent the set of all such subgraph vertex sets constituting G. For each subgraph C, we define the Ising Hamiltonian

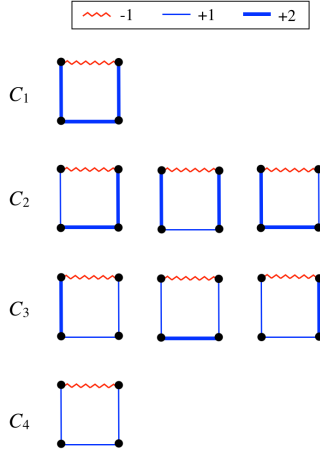$$\mathcal{H}_C = - \sum_{(ij) \in E[C]} J_{ij} s_i s_j \qquad s_i \in \{\pm 1\}, \qquad (1)$$

FIG. 2: Class representatives of the four unit cell subproblem types for square lattices. Red wiggly lines represent antiferromagnetic couplers with value -1, whereas straight blue lines represent ferromagnetic couplers with values $+1$ (thin lines) and $+2$ (thick lines). Black dots represent the spins. Subproblems of class C_i have i ground states, which always includes the all spins up and all spins down state.
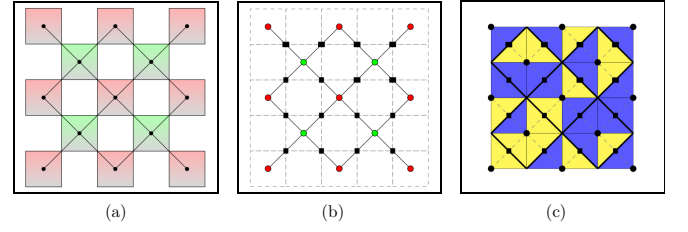

FIG. 3: Steps involved in mapping a planted Ising problem into a tiling puzzle. For clarity, free boundary conditions are used. (a) Construction of the subproblem lattice $\tilde{G}$ by placing a vertex at the center of each planted cell. The domain of each subproblem lattice variable $\mathbf{s}_C$ is the set of ground states of the planted subproblem. (b) The factor graph of $\tilde{G}$, with the factors shown as squares. As discussed in the text, the factors represent the constraints enforced on the subproblem lattice variables due to each Ising spin being shared by two adjacent cells. (c) The Voronoi tessellation of $\tilde{G}$ which yields the set of tiling locations (areas within thick lines). A hypothetical tile is placed at each tiling location. The tile faces are in two colors; blue (dark) and yellow (light); which represent the Ising spin values $+1$ and -1. An optimal solution to the overall problem requires the colors of adjacent tile faces to agree (i.e., the factor constraints to be satisfied). Adapted from Ref. [41].

which will henceforth be referred to as a subproblem Hamiltonian. We then form the complete Ising Hamiltonian $\mathcal{H}$ over graph G by adding all subproblem Hamiltonians as

$$\mathcal{H} = \sum_{C \in \mathcal{C}} \mathcal{H}_C. \qquad (2)$$

As a straightforward result of constructing $\mathcal{H}$ as a direct sum of subproblem Hamiltonians, if all subproblem Hamiltonians share a common ground-state configuration, this state will also be a ground state of the overall Hamiltonian $\mathcal{H}$. Thus, the ground state energy of $\mathcal{H}$ is also known *a priori*. By carefully choosing the couplers for the subproblem Hamiltonians from different classes with varying levels of frustration, one can control the computational hardness of the entire problem to a great extent [41].

We now proceed to define a set of subproblem classes for the square lattice topology. Let us choose the ferromagnetic ground state; i.e., all spins either up or down as the intended shared ground state of the subproblems. Note that once the problem is constructed, one can transform the planted solution from the ferromagnetic ground state to an arbitrary state via a simple gauge transformation. Here we propose four subproblem classes denoted by $\{C_i\}$, $i \in \{1, 2, 3, 4\}$, corresponding to bond configurations on square plaquettes, see the illustration in Fig. 2. For the exchange couplings we use two magnitudes J_l and J_s with $|J_l| > |J_s|$. Here we arbitrarily choose $|J_l| = 2$ and $|J_s| = 1$. The use of two different coupling strengths allows us to tune the degeneracy of the overall optimization problems and hence achieve a variation in hardness of the instances created.

An instance of the subproblem class C_i is constructed as follows. First, a chosen edge of the subproblem unit cell is set to the antiferromagnetic coupler value of $-J_s$. Then we assign the ferromagnetic value $+J_s$ to a randomly-selected set

of $i - 1$ remaining edges, while the rest of the edges are set to $+J_l$. This construction procedure leads to 3 equivalent subproblem representations for the classes C_2 and C_3 and unique representations for C_1 and C_4, up to overall rotations in multiples of 90 degrees of the plaquettes, see Fig. 2. From this construction it is clear that subproblems of class C_i have i different ground states (apart from overall spin reversal), and the ferromagnetic configurations are always ground states.

When generating planted instances, we first choose a subproblem class for each unit cell subproblem (i.e., shaded square plaquettes in Fig. 1) based on a chosen probability distribution over classes $\{C_i\}$. Then for each subproblem, we randomly choose one of the equivalent class representatives shown in Fig. 2, followed by a random rotation of the plaquette to introduce more disorder. We define each instance class based on the chosen probability distribution over the subproblem classes $\{C_i\}$. Let p_i denote the probability of choosing subproblems from class C_i. We can then uniquely identify each instance class in terms of three probability parameters, for instance $\{p_1, p_2, p_3\}$, where $p_1 + p_2 + p_3 \leq 1$. As we demonstrate below, one can induce tremendous variations in problem hardness by tuning the probability parameters $\{p_i\}$. Moreover, due to the simplistic nature of the construction procedure, hundreds of problem instances with moderate system sizes can be generated in seconds with very low computational cost.

We note that all of the subproblems C_i correspond to frustrated squares [48], whereas the remaining plaquettes (white cells in Fig. 1) are randomly frustrated with probability $15/32$, leading to an overall concentration of about 73% frustrated plaquettes in the resulting instances [49]. To study the degeneracy of the full samples resulting from subproblem classes C_i, we use exact enumeration based on the evaluation of Pfaffians which can be achieved in polynomial time for the case

of planar graphs [46]. On its own, subproblem C_i has i ground states and hence $i^{\mathcal{N}}$ is an upper bound to the number of ground states of samples composed of subproblems of class i, where $\mathcal{N}$ is the number of plaquettes (shaded cells in Fig. 1). As a consequence, instances entirely composed of C_1 have a unique ferromagnetic ground state up to overall spin reversal. For the other classes the connection of subproblems provides additional constraints reducing the degeneracy. For example, for $L = 24$ we find the following ground-state entropies $s_0 = S_0/\mathcal{N}$ per shaded plaquette

$$\exp(s_0) = \begin{cases} 1.33(5) & \text{for } C_2 \\ 2.285(2) & \text{for } C_3 \\ 4.018(2) & \text{for } C_4 \ . \end{cases} \quad (3)$$

In comparison, the standard $\pm J$ spin-glass model in two space dimensions has $\exp(s_0) \approx 1.38$, so it turns out to be closest to C_2 in this respect, which as we will see later on provides the hardest samples among the pure classes C_i.

As demonstrated in Ref. [41], the planted problem construction can be translated to a specific type of constraint satisfaction problem called a tiling puzzle [50], a well-known example of which is Eternity II. Figure 3 illustrates the steps involved in the derivation of a tiling puzzle from the unit cell planting formulation. As shown in Fig. 3(a), we first construct a graph with respect to $\mathcal{C}$ (which we call the subproblem lattice $\tilde{G}$) by placing a vertex at the center of each planted cell. Each pair of vertices in $\tilde{G}$ is considered adjacent if and only if the corresponding subgraphs (shaded cells) share a corner vertex. Let us associate each vertex in $\tilde{G}$ with a subproblem lattice variable $\mathbf{s}_C$ over the four Ising variables of the corresponding subproblem. The domain of $\mathbf{s}_C$ is the set of ground states of the subproblem. However, viable solutions to $\mathbf{s}_C$ are constrained by the equality conditions enforced on the shared Ising variables. That is, for two neighboring cells C and C' with a shared corner vertex i, $s_C^i = s_{C'}^i$. A solution to the overall problem should simultaneously satisfy all such equality constraints. By interpreting each equality constraint as a factor over the subproblem lattice variables $\mathbf{s}_C$ and $\mathbf{s}_{C'}$, one can construct a factor graph [51] associated with $\tilde{G}$ as shown in Fig. 3(b), where the factors are represented by squares. We then perform a Voronoi tessellation [52] of $\tilde{G}$ [Fig. 3(c)] which partitions the surrounding space into a set of tilted square regions centered at each vertex, whose boundaries are shown in thick lines. We can interpret each region as a tiling location, with an allowable set of tiles and orientations as determined by the domain of $\mathbf{s}_C$ (the ground state set of the subproblem). In Fig. 3(c), a hypothetical tile is placed at each location, where blue (dark) and yellow (light) tile faces represent the two Ising spin values ($+1$ and -1). The optimal solution to the overall problem can now be interpreted as finding a tile arrangement in which no two adjacent tile faces have a different color; i.e., all factor constraints are satisfied.

III. RESULTS

A. Simulation details

To compare the typical hardness of planted instances across different problem classes, we primarily use population annealing Monte Carlo [14–17, 53, 54]. For certain regimes with interesting variations in hardness, we also use simulated annealing (SA) [8] and simulated quantum annealing (SQA) [18–21].

Population annealing Monte Carlo (PAMC) is a sequential Monte Carlo algorithm somewhat similar in spirit to simulated annealing (SA). In contrast to the latter, however, PAMC was designed with equilibrium simulations in mind, and not as an optimization method. It considers an ensemble of copies of the same system and disorder realization that is started at a high temperature and successively cooled down to the lowest temperatures of interest. In addition to equilibrating update steps applied to each copy that are typically implemented as Markov Chain Monte Carlo (MCMC), the population is further relaxed on lowering the temperature by a resampling step that selects and replicates (or eliminates) copies proportional to their relative Boltzmann weight at the new temperature. Large fluctuations in the weights that determine resampling are a signature of the difficulty in equilibrating a given system [15] and lead to the descendants of only a few original copies dominating the population. Hence, a measure of the effective number of surviving replica families at the lowest temperature allows one to distinguish between hard and easy problems within the instance classes. If n_i is the fraction of the population descended from replica i in the initial population (i.e., the size of the ith family), the entropic family size ρ_s [16] is given by

$$\rho_s = \lim_{R \to \infty} R \, e^{\sum_i n_i \log n_i}, \quad (4)$$

where R is the initial population size. For a given set of simulation parameters, the larger the value of ρ_s, the smaller the number of surviving families, and hence the more rugged the problem's energy landscape. Thus, ρ_s provides a measure of hardness for algorithms that are based on local search in the classical energy landscape. As was shown previously, ρ_s is highly correlated with other well established hardness metrics such as the integrated autocorrelation time in Markov-chain Monte Carlo and, specifically, in parallel tempering (PT) Monte Carlo [16]. A unique advantage of ρ_s is that it can be measured with relatively low computational cost in comparison to PT autocorrelation times, as well as metrics based on optimized time-to-solution [55]. This allows us to rigorously investigate a large region of the instance class parameter space that results from random selection of subproblem types.

Table I shows the PAMC simulation parameters for the three linear system sizes used in our study to characterize hardness, $L = 16$, $L = 24$, and $L = 32$. ρ_s is known to converge with increasing populating size R, and R values for different system sizes were chosen accordingly to ensure that this convergence criterion is met by all simulations.

In addition to PAMC simulations, we also perform SA and

TABLE I: Parameters for the population annealing Monte Carlo simulations. L is the linear system size, R is the number of replicas, T_0 is the lowest temperature, and N_T is the number of temperature steps. At each temperature step, $N_S = 10$ Monte Carlo sweeps per temperature step are performed on each replica. The annealing schedule is linear in the inverse temperature.

L	R	T_0	N_T
16	1×10^5	0.2	301
24	2×10^5	0.2	301
32	1×10^6	0.2	301

SQA calculations on a selected subset of problem classes. SA calculations are performed with the optimized multi-spin code by Isakov *et al.* [56], using a linear annealing schedule with an initial temperature of $T_i = 10$ and a final temperature of $T_f = 0.2$. For the SQA calculations, we use 64 Trotter slices and a temperature of $T = 0.03125$, while linearly decreasing the transverse field magnitude from $\Gamma = 2.5$ to 0. For both SA and SQA we estimate the time required to find the optimal solution at least once with probability p_d, i.e., the time-to-solution [57, 58]

$$\text{TTS}(t_A) = t_A \frac{\log(1 - p_d)}{\log[1 - p_s(t_A)]}, \tag{5}$$

where t_A is the annealing time and p_s is the success probability, while $p_d = 0.99$. We measure the TTS for individual problem instances, and then calculate the median of the distribution of TTS values for a given instance class and system size. We minimize the median TTS in annealing time t_A to obtain the optimal median TTS which takes into account the best tradeoff between the annealing time and the number of independent runs [57]. For simplicity, hereafter we use the term time-to-solution (TTS) to refer to the aforementioned *optimal median* TTS obtained for each instance class and system size.

Finally, to gain insight into the physical mechanisms of hardness, we investigate thermodynamic properties of a selected subset of instance classes using PAMC, as well as using the Pfaffian enumeration method of Ref. [46] to determine the exact density of states and hence exact thermodynamic averages for energetic quantities for each sample. Via PAMC simulations, we measure the Binder ratio g_O via

$$g_O = \frac{1}{2}\left(3 - [\langle O^4 \rangle]_{\text{av}} / [\langle O^2 \rangle]_{\text{av}}^2\right), \tag{6}$$

where the order parameter O represents either the magnetization $m = (1/N)\sum_i s_i$ (ferromagnetic order), or the spin overlap $q = (1/N)\sum_i s_i^\alpha s_i^\beta$ (spin-glass order), with α and β representing two independent replicas of the system with the same disorder. Note that $\langle \cdots \rangle$ and $[\cdots]_{\text{av}}$ represent thermal average and disorder average, respectively. As a dimensionless quantity, the Binder ratios for different system sizes are expected to cross close to the point of a continuous phase transition. From the expected scaling behavior [59],

$$g_O \sim G_O[L^{1/\nu_O}(T - T_c)], \tag{7}$$

it is straightforward to extract the critical temperature T_c and the critical exponent ν_O from a scaling collapse [60, 61]. In addition to the Binder ratio, we also investigate the specific heat,

$$C_v = 1/(k_B T^2 N)[\langle \mathcal{H}^2 \rangle - \langle \mathcal{H} \rangle^2]_{\text{av}}, \tag{8}$$

using the planar graph solver, which provides us with a measure free of statistical errors.

B. Base instance classes

We first focus on problems constructed using subproblems drawn from a single subproblem class. Let us refer to the resulting four instance classes as base classes. Figure 4 shows the distributions of $\log_{10} \rho_s$ for the four base classes, along with the results for random bimodal spin glasses, i.e., $J_{ij} \in \{\pm 1\}$. For the bimodal instances, we use the same PAMC simulation parameters as used for the base classes. As Fig. 4 shows, ρ_s has a very broad distribution such that the distribution of $\log_{10} \rho_s$ is at least similar to a normal shape, and we hence use $\log_{10} \rho_s$ as our preferred form of the hardness metric.

Figure 4 shows that both the C_2 base class and the bimodal class have very broad distributions, with the bimodal distribution being strongly skewed towards hard problem instances. In contrast, the C_3 and C_4 base classes have quite narrow distributions which appear to have vanishing overlap with the bimodal case, clearly indicating that the problems belonging to these classes are easier than the bimodal spin glasses. C_4 has the leftmost distribution among all classes, and hence produces the easiest instances, at least according to the ρ_s metric. On the other hand, the distribution for C_2 lies the farthest to the right, only overlapping with the tail of the bimodal distribution. Thus, we can conclude that C_2 instances are at least as hard as the hardest instances belonging to the bimodal class. Finally, based on the ρ_s hardness metric, we can list the four base classes in sequence according to increasing order of hardness as C_4, C_3, C_1, and C_2. We will later demonstrate that by mixing the four subproblem types, one can construct problems with varying degrees of complexity, with the level of hardness as measured by ρ_s lying between those of the C_4 and C_2 base classes.

Before we proceed to problems constructed using mixtures of subproblem types, let us investigate thermodynamic properties of the base classes to uncover any noteworthy behavior such as the presence of phase transitions. We first present results for the C_3 and C_4 classes due to their trivial thermodynamic behavior in comparison to other base classes. Figure 5(a) shows the specific heat C_v and Fig. 5(b) the Binder ratio g_q as functions of temperature for the C_3 base class. In Fig. 6 we present the same quantities for the C_4 base class. Here, the specific heat is determined using the planar graph solver [46] whereas the magnetization and the Binder ratio are measured using PAMC simulations. For the PAMC simulations, the results for system sizes $L = 16$, 24, and 32 were generated using the parameters presented in Table I. For $L = 10$, we use $R = 1 \times 10^5$ and $T = 201$, and for $L = 48$,
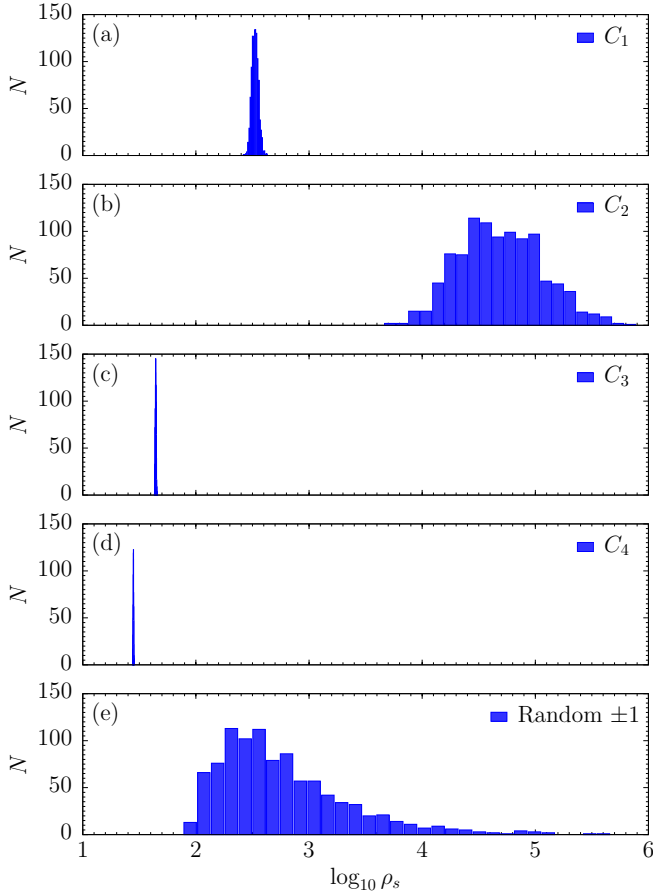
FIG. 4: Distributions of the logarithm of the entropic family size, $\log_{10} \rho_s$, for planted problems with system size $L = 32$ constructed using subproblems drawn from a single subproblem type: (a) C_1, (b) C_2, (c) C_3, and (d) C_4. Panel (e) shows the distribution of $\log_{10} \rho_s$ for bimodal spin glasses with $J_{ij} \in \{\pm 1\}$. In each case, 1000 instances per class were used.

we use $R = 2 \times 10^5$ and $T = 401$, with $T_0 = 0.2$ and $N_S = 10$ for both cases. To ensure thermal equilibration, we require the condition $R/\rho_s > 100$ [16] to be met, and when it is not satisfied by an instance, it is rerun by increasing the number of temperature steps N_T. As is demonstrated in Figs. 5 and 6, the specific heat for both C_3 and C_4 classes does not show any system-size dependence. Moreover, the Binder cumulants g_q for different system sizes do not show any sign of an intersection, indicating the absence of ferromagnetic or spin-glass transitions in these two base classes, which hence show properties characteristic of disordered spin systems in dimensions below the lower critical dimension. The implied absence of critical slowing down and any significant barriers in the free-energy landscape results in the relative ease of equilibrating the samples that is reflected in the small values of ρ_s shown in Fig. 4.

In Fig. 7, we present results for the specific heat C_v, the average magnetization $[\langle |m| \rangle]_{\mathrm{av}}$, and the Binder ratio g_m for the C_1 base class. The specific heat and the average magnetization resemble that of the ferromagnetic Ising model,
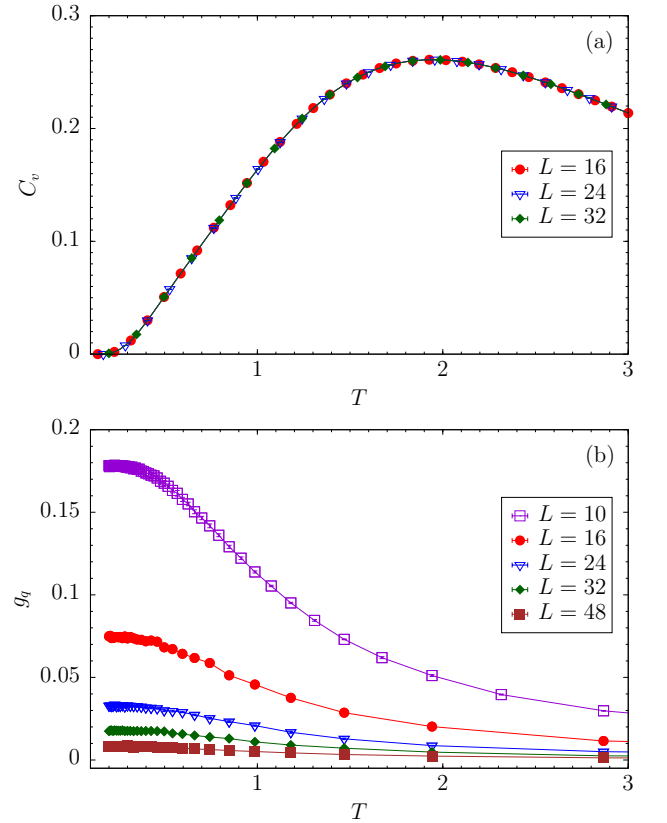

FIG. 5: (a) The specific heat C_v and (b) the Binder ratio g_q as functions of temperature for the C_3 base class. The curves are for different system sizes. The size independence of the specific heat and lack of intersections of the Binder cumulants clearly indicate the absence of a thermodynamic phase transition.

with a logarithmic divergence of C_v and the magnetization scaling to zero at the transition point $\sim (T - T_c)^{1/8}$ [62]. Moreover, the Binder parameter g_m for different system sizes clearly intersect at a common temperature T_c. Using a scaling collapse [61], we determine the critical temperature to be $T_c = 1.834(2)$, with $\nu_m = 1.001(5)$. Our results indicate that despite being a disordered and frustrated system, the C_1 base class has predominantly ferromagnetic features. This ferromagnetic ordering is a necessary consequence of the fact that these instances only have a single ground state (excluding spin-flip symmetry), which is the planted ferromagnetic solution.

Finally, we explore properties of the C_2 base class. In Fig. 8, we show the specific heat C_v, magnetization $[\langle |m| \rangle]_{\mathrm{av}}$, and Binder parameter g_m for the C_2 class. Figure 8(c) shows that g_m for different system sizes intersect in the temperature interval $T \in (0.4, 0.55)$, which indicates that some ferromagnetic ordering occurs. The fact that the curves do not intersect at a common point indicates that corrections to scaling are significant for these system sizes. Hence, we do not attempt to extract the critical temperature via a scaling analysis. The average magnetization [Fig. 8(b)] also shows features reminiscent of a ferromagnetic transition, although as $T \to 0$,

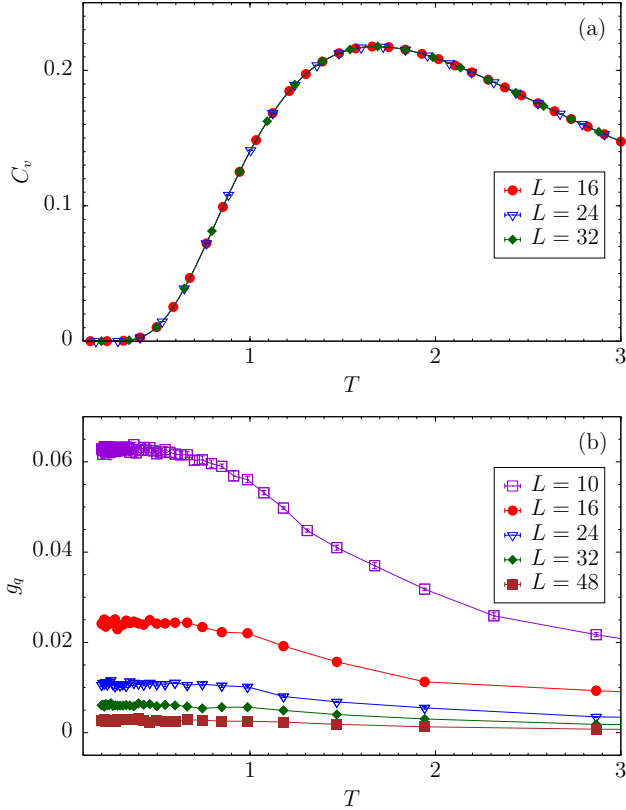FIG. 6: Same as Fig. 5, but for the C_4 base class. Again, there is no sign of a phase transition.

FIG. 7: (a) Specific heat C_v, (b) average magnetization $[\langle|m|\rangle]_{\text{av}}$, and (c) Binder parameter g_m as functions of temperature T for the C_1 base class. The curves are for different system sizes. The curves for g_m for different system sizes cross at a common finite temperature $T_c = 1.834(2)$, which indicates a ferromagnetic phase transition.

$[\langle|m|\rangle]_{\text{av}}$ appears to approach a value close to 0.8, rather than 1.0 as in the case of the ferromagnetic Ising model. The specific heat [Fig. 8(a)] does not show a discernible system-size dependence, at least for the system sizes considered.

This peculiar ordering behavior can be understood by considering the clustering behavior of strong-ferromagnetic ($+2$) bonds in C_2 instances. In C_2 instances, 50% of the couplers are $+2$ bonds. By investigating the percolation properties of $+2$ bonds, we find that the spanning probability asymptotically approaches unity in the thermodynamic limit. This indicates that the lattice is in the percolating phase, and that in the thermodynamic limit, there is a nonvanishing fraction of sites in the largest cluster of $+2$ bonds. We find that for the lattice sizes considered, approximately 80% of the spins belong to the largest bond cluster. Note that this is in contrast to an *uncorrelated* percolation problem in its ordered phase, where close to 100% of lattice sites would belong to the percolating cluster. The remaining spins either belong to smaller $+2$-bond clusters scattered around the lattice, or they are isolated sites with no $+2$ bonds attached, see Fig. 9 for an illustration. Due to intrinsic properties of the C_2 lattices, $+2$-bond clusters and "isolated" spins have equal number of weak-ferromagnetic ($+1$) and weak-antiferromagnetic (-1) bonds attached. As a result, the flipping of an isolated spin, or the simultaneous flipping of all the spins in a $+2$-bond cluster, leaves the energy unchanged. By examining the
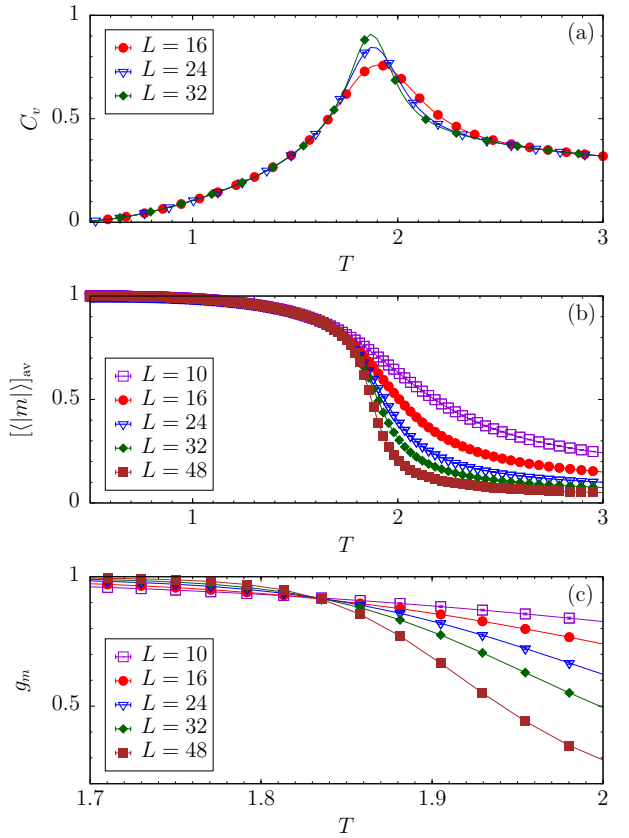
ground-state spin configurations, we find that all $+2$ bonds are satisfied in the ground state, that is, spins within each cluster are aligned with one another. Thus, the ground state degeneracy in C_2 instances arises from the energy-free flipping of entire clusters or isolated spins. As the critical temperature is approached from above, each cluster would undergo a transition from a randomly-oriented (paramagnetic) state to a ferromagnetically aligned state. This is demonstrated in Fig. 10, where we show the average magnetization $\langle|m|\rangle$ as a function of temperature for the three largest clusters of a single C_2 instance. As $T \to 0$, we observe that $\langle|m|\rangle \to 1$ as the spins within each cluster are ferromagnetically aligned.

A main factor leading to the observed hardness in C_2 instances is the critical slowing down that occurs as the system undergoes a ferromagnetic transition at a considerably low temperature $T \in (0.4, 0.55)$. We point out that cluster algorithms [63, 64] could be effective in reducing critical slowing down and improving the performance. However, an analysis on the performance of problem-specific algorithms is beyond the scope of this paper, and hence was not attempted. The predominantly ferromagnetic nature of C_1 and C_2 base-class instances is not surprising when considering the fraction of strong-ferromagnetic bonds in C_1 and C_2 plaquettes. Three
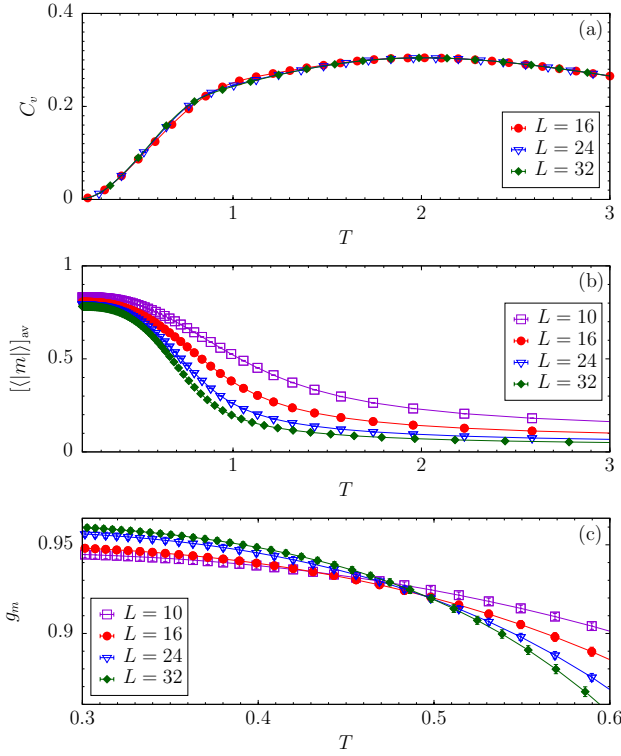
FIG. 8: (a) Specific heat C_v, (b) average magnetization $[\langle |m| \rangle]_{\rm av}$, and (c) Binder parameter g_m as functions of temperature T for the C_2 base class. The curves are for different system sizes.
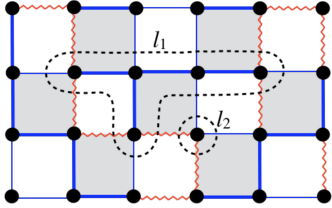

FIG. 9: A section of the lattice structure of a C_2 base class instance. Red wiggly lines represent antiferromagnetic couplers with value -1, whereas straight blue lines represent ferromagnetic couplers with values $+1$ (thin lines) and $+2$ (thick lines). The loop l_1 encloses a cluster of strong-ferromagnetic ($+2$) bonds, while l_2 encloses an "isolated" spin with no $+2$ bonds attached. Due to intrinsic properties of the C_2 lattice structure, $+2$-bond clusters and isolated spins in C_2 instances have equal number of $+1$ and -1 bonds attached. Thus, the flipping of an isolated spin, or the simultaneous flipping of all the spins in a $+2$-bond cluster, preserves energy.

out of four bonds in a C_1 plaquette are strong-ferromagnetic bonds, and, therefore, C_1 instances have the strongest ferromagnetic properties among all classes. With the replacement of each strong-ferromagnetic bond with a weak-ferromagnetic bond, the plaquettes progressively become less ferromagnetic and more frustrated in the order $C_1 \rightarrow C_2 \rightarrow C_3 \rightarrow C_4$. While both C_1 and C_2 order ferromagnetically with the accompanying critical slowing down, C_2 also shows a significant ground-state degeneracy [cf. Eq. (3)], and the expected
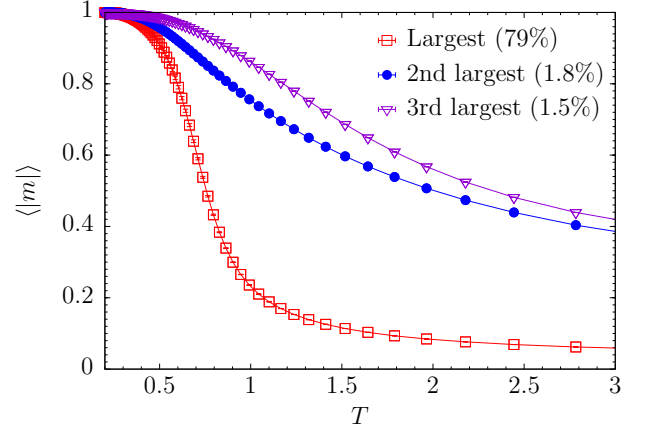

FIG. 10: Average magnetization $\langle |m| \rangle$ as a function of temperature for the three largest clusters of strong-ferromagnetic ($+2$) bonds of a single C_2 base class instance ($L = 32$). The largest cluster comprises of 79% of the spins in the lattice, while the second and third largest clusters, respectively, contain 1.8% and 1.5% of the spins.

energy barriers between the multitude of ground states lead to additional slow dynamics at low temperatures that is absent for C_1, explaining the much weaker computational challenge provided by C_1 instances as compared to C_2 samples.

C. Mixtures of two subproblem types

We now investigate planted instances constructed using subproblems drawn from two plaquette types. Here we focus on two regimes where interesting variations in hardness can be observed: mixtures of C_1 and C_3 plaquettes, and mixtures of C_1 and C_4 plaquettes. Rather than comparing $\log_{10} \rho_s$ distributions, here we consider the disorder averages $\langle \log_{10} \rho_s \rangle$ computed over 200 problems drawn from each instance class per system size. Figure 11(a) shows $\langle \log_{10} \rho_s \rangle$ for C_1–C_3 plaquette mixtures plotted as a function of p_1, which is the probability of choosing subproblems from class C_1. Thus, $p_1 = 1$ corresponds to the instance class with all subproblems drawn from C_1 plaquette type (C_1 base class), whereas $p_1 = 0$ represents instances with all C_3 subproblems (C_3 base class). Results are shown for three system sizes, $L = 16$, $L = 24$, and $L = 32$. Figures 11(b) and 11(c) show the optimized median TTS for SA and SQA estimated using 200 problems. Figure 12 shows the same quantities for C_1–C_4 plaquette mixtures. Results from all three algorithms clearly indicate peaks in problem hardness at $p_1 \approx 0.35$ for C_1–C_3 mixtures, and $p_1 \approx 0.45$ for C_1–C_4 mixtures, i.e., an easy-hard-easy transition. This easy-hard-easy transition is akin to the phase transition one observes in Boolean satisfiability (k-SAT) problems at a certain clauses-to-variables ratio, below which the formula is satisfiable and above which it is unsatisfiable [65]. A similar hardness peak has been observed for the frustrated loop problems on the Chimera lattice as the loop density is varied [36].

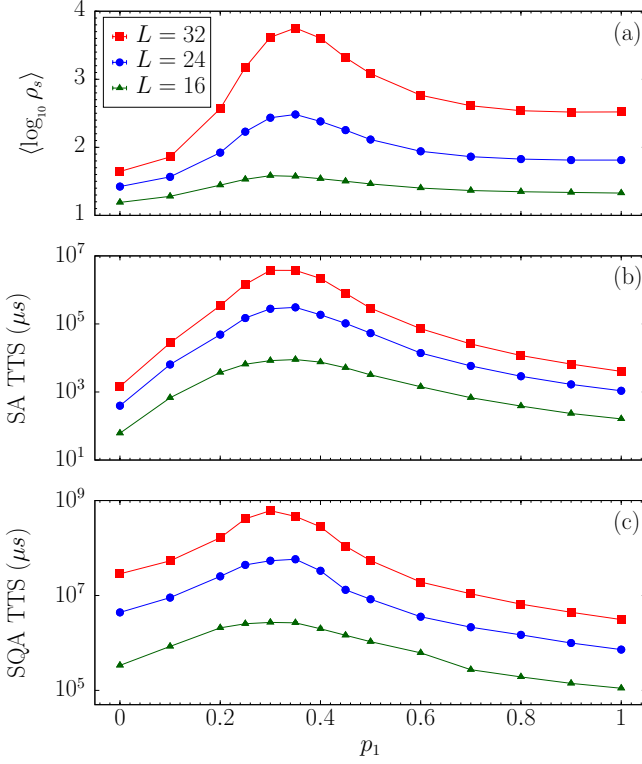It is interesting to explore whether these hardness peaks co-

FIG. 11: (a) Population annealing $\langle \log_{10} \rho_s \rangle$, (b) simulated annealing optimal median TTS, and (c) simulated quantum annealing optimal median TTS for instance classes comprised of mixtures of C_1 and C_3 subproblem types. The results are plotted against p_1, which is the probability of choosing subproblems from class C_1. The curves are for three system sizes, $L = 16$, $L = 24$, and $L = 32$. $\langle \log_{10} \rho_s \rangle$ and median TTS values are estimated using 200 problems per instance class, per system size. All panels have the same horizontal scale.
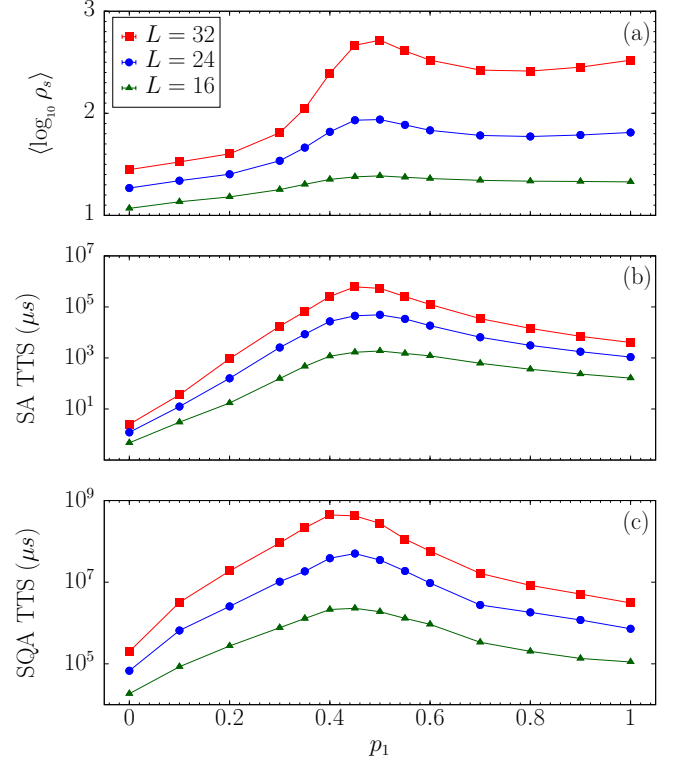
FIG. 12: (a) Population annealing $\langle \log_{10} \rho_s \rangle$, (b) simulated annealing optimal median TTS, and (c) simulated quantum annealing optimal median TTS for instance classes comprised of mixtures of C_1 and C_4 subproblem types. The results are plotted against p_1, which is the probability of choosing subproblems from class C_1. The curves are for three system sizes, $L = 16$, $L = 24$, and $L = 32$. $\langle \log_{10} \rho_s \rangle$ and median TTS values are estimated using 200 problems per instance class, per system size. All panels have the same horizontal scale.

incide with, or, are driven by thermodynamic phase transitions. Based on the thermodynamic behavior of the instance classes at $p_1 = 0$ (C_3 and C_4) and $p_1 = 1$ (C_1), it is reasonable to speculate that at zero temperature, as p_1 is varied from 0 to 1, the system may undergo a transition from a disordered phase to a ferromagnetic phase. To further explore this hypothesis, we focus on the C_1–C_3 plaquette mixtures and measure $[\langle |m| \rangle]_{\mathrm{av}}$ and g_m at the lowest temperature $T_{\min} = 0.2$ for different values of $p_1 \in [0, 1]$. The results are shown in Fig. 13 as a function of p_1, where Fig. 13(a) shows $[\langle |m| \rangle]_{\mathrm{av}}$ and Fig. 13(b) shows the quantity $Q_m = -\ln(1 - g_m)$. Here, the quantity $Q_m = -\ln(1 - g_m)$ was chosen over g_m as it has a smaller curvature near the transition [66], allowing for a more accurate estimation of the crossing point. Figure 13(a) shows that $[\langle |m| \rangle]_{\mathrm{av}} \rightarrow 1$ as $p_1 \rightarrow 1$, consistent with the ferromagnetic properties of the C_1 base class. As Fig. 13(b) shows, Q_m for different system sizes intersect at a nonzero p_1 value, further confirming the presence of a ferromagnetic transition. Assuming a scaling behavior of the form $Q_m \sim F[L^{1/\kappa}(p_1 - p_1^c)]$, we perform a finite-size scaling analysis and determine the point of intersection to be $p_1^c = 0.347(8)$, with $\kappa = 1.8(1)$ [67]. Based on the hard-

ness peak positions of $\langle \log_{10} \rho_s \rangle$ for $L = 16$, 24, and 32 [see Fig. 11(a)], we determine the asymptotic value of the peak position as $L \rightarrow \infty$ to be $p_1^h = 0.370(6)$, where we have estimated the error bar using bootstrap resampling. The close proximity of the transition point p_1^c to the asymptotic hardness peak position p_1^h clearly indicates that the hardness transition is, indeed, driven by the ferromagnetic transition.

It is noteworthy to mention that apart from the thermodynamic properties, we have also analyzed some heuristic rules based on local measures of frustration [68], but these quantities proved not to be predictive of the hardness transitions or the relative levels of hardness of the base classes [69].

A comparison of results for different solvers in Fig. 11 reveals another interesting feature with regard to the hardness of C_1 and C_3 base classes. According to the two classical algorithms PAMC and SA, instances from C_1 base class are harder than those from C_3 class, as conveyed by relatively higher values of $\langle \log_{10} \rho_s \rangle$ and SA TTS. However, SQA TTS for C_1 base class is lower than that for C_3 class, indicating that SQA finds C_1 base class instances easier to solve than C_3 instances. On the other hand, when comparing the solver performances for C_1 and C_4 plaquette combinations (Fig. 12),
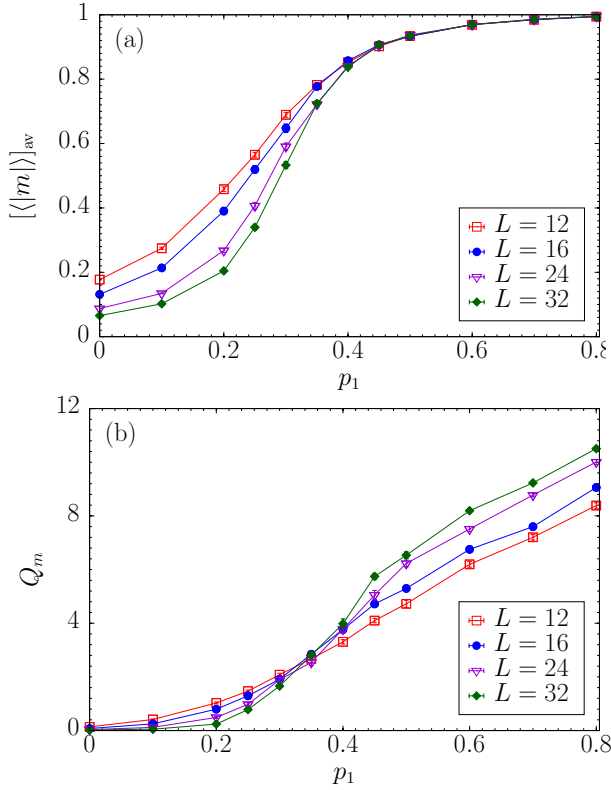
FIG. 13: (a) Average magnetization $[\langle|m|\rangle]_{\mathrm{av}}$ and (b) $Q_m = -\ln(1 - g_m)$ for C_1–C_3 instance classes, measured at the lowest temperature simulated, $T_{\min} = 0.2$. The horizontal axis represents p_1.
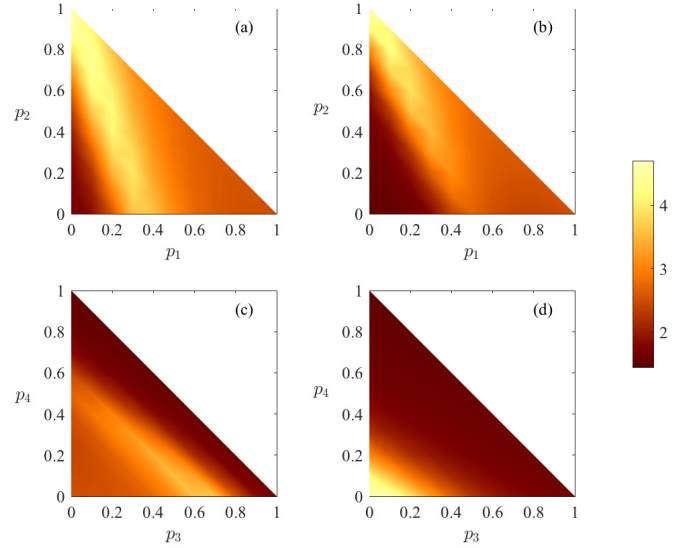

FIG. 14: Heat maps of $\langle\log_{10}\rho_s\rangle$ for instance classes comprised of mixtures of three subproblem types: (a) C_1–C_2–C_3 mixtures, (b) C_1–C_2–C_4 mixtures, (c) C_1–C_3–C_4 mixtures, and (d) C_2–C_3–C_4 mixtures. The results are for system size $L = 32$. Simulations were performed for a finite set of instance classes defined on a discrete grid with each probability parameter p_i incremented by a step size of 0.1. For each of those instance classes, $\langle\log_{10}\rho_s\rangle$ is obtained by averaging over the results of 200 instances and depicted as a color hue. $\langle\log_{10}\rho_s\rangle$ values for intermediate points in the parameter space are estimated through interpolation.

one finds that the ordering of hardness levels for C_1 and C_4 base classes is consistent across all three solvers, that is, C_4 instances being easier than C_1 instances.

D. Mixtures of three subproblem types

Finally, we explore variations in problem hardness among instance classes constructed using three subproblem types. Here we discretize the parameter space into a grid by incrementing each probability parameter p_i by a step size of 0.1. We perform PAMC simulations for the instance classes defined on the grid points that represent mixtures of three subproblem types. $\langle\log_{10}\rho_s\rangle$ is computed by averaging over 200 problems per instance class. Figure 14 shows $\langle\log_{10}\rho_s\rangle$ for $L = 32$ for the four types of three-plaquette combinations: C_1–C_2–C_3 [Fig. 14(a)], C_1–C_2–C_4 [Fig. 14(b)], C_1–C_3–C_4 [Fig. 14(c)], and C_2–C_3–C_4 [Fig. 14(d)]. The results are represented as heat maps, with $\langle\log_{10}\rho_s\rangle$ for the points between the grid points estimated via interpolation. x and y axes in each plot represent two of the free probability parameters that uniquely define instance classes in the mixture. The color grade from dark red to light yellow represents low (red/dark) to high (yellow/light) values of $\langle\log_{10}\rho_s\rangle$.

First focusing on C_1–C_2–C_3 [Fig. 14(a)] and C_1–C_2–C_4 [Fig. 14(b)] mixtures, we note that $p_2 = 0$ in Fig. 14(a) and

Fig. 14(b), respectively, correspond to C_1–C_3 and C_1–C_4 plaquette mixtures investigated in Sec. III C. For any fixed value of p_2, as p_1 approaches from 0 to 1, one observes a change in the color grade of the form dark $\rightarrow$ light $\rightarrow$ dark, which corresponds to an easy-hard-easy transition. Thus, the hardness transitions discussed in Sec. III C for the case of $p_2 = 0$ are also prevalent for nonzero p_2 in the multidimensional parameter space of three-plaquette combinations. We also observe that the hardness increases with increasing p_2, which is corroborated by the fact that C_2 plaquettes present the hardest base class. Increasing the fraction of C_2 plaquettes would thus increase the problem difficulty.

Another hardness transition can be observed in the parameter space of C_1–C_3–C_4 plaquette mixtures [Fig. 14(c)], as either p_3 or p_4 approaches from 0 to 1 (or, equivalently, when decreasing p_1 from 1 to 0). $\langle\log_{10}\rho_s\rangle$ for C_2–C_3–C_4 mixtures [Fig. 14(d)], however, does not show evidence for a hardness transition in the corresponding parameter space. The hardness seems to monotonically increase as either p_3 or p_4 is decreased, or in other words, as the fraction of C_2 plaquettes is increased. When comparing the results of all four cases, it is evident that the hardness transitions are observed only in the presence of C_1 plaquettes. Generalizing our conclusions on the C_1–C_3 phase transition to the entire parameter space, we claim that the system passes through a ferromagnetic transition as the fraction of C_1 plaquettes is increased, which manifests itself as a hardness transition in the cases where the hard-

ness is not dominated by a higher concentration of C_2 plaquettes.

Based on the results of all four types of three-plaquette mixtures, we identify that for the system sizes considered, $\langle \log_{10} \rho_s \rangle$ for all instance classes are bounded by those of C_4 (lowest value) and C_2 (highest value) base classes. As a final note, we point out that the quantitative comparison of hardness levels across different instance classes as characterized by $\langle \log_{10} \rho_s \rangle$ may not exactly carry over to other solvers. Exploring the entire parameter space with other solvers using a TTS based metric is not practical due to the sheer number of instance classes involved, and thus was not attempted. However, we believe that the general trends in hardness we observe through $\langle \log_{10} \rho_s \rangle$, such as the hardness transitions, are common among the solvers considered here and, more general, quantum-inspired optimization techniques. This is corroborated by the comparison of multiple solver performances presented in Sec. III C for two sub-regions of the parameter space, where all three algorithms confirm the presence of hardness transitions.

IV. SUMMARY

We have investigated the computational hardness of planted spin-glass problems on a square-lattice topology generated by the method of "tile planting." Our planting scheme is based on partitioning the underlying problem graph into edge-disjoint subgraphs, and embedding subproblems chosen from predefined classes over the subgraphs. The method allows for the fine tuning of problem hardness, from problems quite easier than the typical bimodal spin-glasses, to problems with difficulty levels comparable to the hardest of bimodal spin-glass instances. Using the population annealing Monte Carlo method, we have mapped out a large region of the hardness phase space. We have identified several hardness transitions in the phase space, the origin of which we attribute to underlying ferromagnetic phase transitions. Due to the highly tunable hardness, scalability, and ease of implementation, we believe that this method could be very useful for generating benchmark problems for novel optimization methods implemented both in hardware and software.

[1] A. Gibbons, *Algorithmic Graph Theory* (Cambridge University Press, Cambridge, 1985).

[2] A. Lucas, Front. Physics **12**, 5 (2014).

[3] D. L. Stein and C. M. Newman, *Spin Glasses and Complexity*, Primers in Complex Systems (Princeton University Press, Princeton NJ, 2013).

[4] K. Binder and A. P. Young, Rev. Mod. Phys. **58**, 801 (1986).

[5] F. Barahona, J. Phys. A **15**, 3241 (1982).

[6] F. Krzakała, A. Montanari, F. Ricci-Tersenghi, G. Semerjian, and L. Zdeborová, PNAS **104**, 10318 (2007).

[7] A. K. Hartmann and M. Weigt, *Phase Transitions in Combinatorial Optimization Problems: Basics, Algorithms and Statistical Mechanics* (Wiley-VCH, Berlin, 2005).

[8] S. Kirkpatrick, C. D. Gelatt, Jr., and M. P. Vecchi, Science **220**, 671 (1983).

[9] R. H. Swendsen and J.-S. Wang, Phys. Rev. Lett. **57**, 2607 (1986).

[10] C. Geyer, in *23rd Symposium on the Interface*, edited by E. M. Keramidas (Interface Foundation, Fairfax Station, VA, 1991), p. 156.

[11] E. Marinari and G. Parisi, Europhys. Lett. **19**, 451 (1992).

[12] K. Hukushima and K. Nemoto, J. Phys. Soc. Jpn. **65**, 1604 (1996).

[13] H. G. Katzgraber, S. Trebst, D. A. Huse, and M. Troyer, J. Stat. Mech. P03018 (2006).

[14] K. Hukushima and Y. Iba, in *The Monte Carlo method in the physical sciences: celebrating the 50th anniversary of the Metropolis algorithm*, edited by J. E. Gubernatis (AIP, Los Alamos, New Mexico (USA), 2003), vol. 690, p. 200.

[15] J. Machta, Phys. Rev. E **82**, 026704 (2010).

[16] W. Wang, J. Machta, and H. G. Katzgraber, Phys. Rev. E **92**, 063307 (2015).

[17] W. Wang, J. Machta, and H. G. Katzgraber, Phys. Rev. E **92**, 013303 (2015).

[18] A. B. Finnila, M. A. Gomez, C. Sebenik, C. Stenson, and J. D. Doll, Chem. Phys. Lett. **219**, 343 (1994).

[19] T. Kadowaki and H. Nishimori, Phys. Rev. E **58**, 5355 (1998).

[20] G. Santoro, E. Martoňák, R. Tosatti, and R. Car, Science **295**, 2427 (2002).

[21] B. Heim, T. F. Rønnow, S. V. Isakov, and M. Troyer, Science **348**, 215 (2015).

[22] M. W. Johnson, M. H. S. Amin, S. Gildert, T. Lanting,

F. Hamze, N. Dickson, R. Harris, A. J. Berkley, J. Johansson, P. Bunyk, et al., Nature **473**, 194 (2011).

[23] P. Bunyk, E. Hoskinson, M. W. Johnson, E. Tolkacheva, F. Altomare, A. J. Berkley, R. Harris, J. P. Hilton, T. Lanting, and J. Whittaker, IEEE Trans. Appl. Supercond. **24**, 1 (2014).

[24] K. L. Pudenz, T. Albash, and D. A. Lidar, Nat. Commun. **5**, 3243 (2014).

[25] K. L. Pudenz, T. Albash, and D. A. Lidar, Phys. Rev. A **91**, 042302 (2015).

[26] Z. Zhu, A. J. Ochoa, F. Hamze, S. Schnabel, and H. G. Katzgraber, Phys. Rev. A **93**, 012317 (2016).

[27] S. Mandrá and H. G. Katzgraber, Quantum Sci. Technol. **3**, 04LT01 (2018).

[28] T. Albash and D. A. Lidar, Phys. Rev. X **8**, 031016 (2018).

[29] Z. Wang, A. Marandi, K. Wen, R. L. Byer, and Y. Yamamoto, Phys. Rev. A **88**, 063853 (2013).

[30] R. Hamerly, T. Inagaki, P. L. McMahon, D. Venturelli, A. Marandi, T. Onodera, E. Ng, C. Langrock, K. Inaba, T. Honjo, et al. (2018), (arXiv:quant-phys/1805.05217).

[31] S. Matsubara, H. Tamura, M. Takatsu, D. Yoo, B. Vatankhahghadim, H. Yamasaki, T. Miyazawa, S. Tsukamoto, Y. Watanabe, K. Takemoto, et al., in *Complex, Intelligent, and Software Intensive Systems – Proceedings of the 11th International Conference on Complex, Intelligent, and Software Intensive Systems (CISIS-2017), Torino, Italy, July 10–12, 2017* (2017), p. 432.

[32] S. Tsukamoto, M. Takatsu, S. Matsubara, and H. Tamura, FUJITSU Sci. Tech. J. **53**, 8 (2017).

[33] M. Aramon, G. Rosenberg, T. Miyazawa, H. Tamura, and H. G. Katzgraber, Front. Phys. **7**, 48 (2019).

[34] In this work, statements about "hardness" refer to empirically-observed difficulty faced by a considered class of algorithms rather than a characterization in terms of the classes of computational complexity theory.

[35] W. Barthel, A. K. Hartmann, M. Leone, F. Ricci-Tersenghi, M. Weigt, and R. Zecchina, Phys. Rev. Lett. **88**, 188701 (2002).

[36] I. Hen, J. Job, T. Albash, T. F. Rønnow, M. Troyer, and D. A. Lidar, Phys. Rev. A **92**, 042325 (2015).

[37] A. D. King, T. Lanting, and R. Harris (2015), arXiv:1502.02098.

[38] C. Coffrin, H. Nagarajan, and R. Bent, in *Integration of Constraint Programming, Artificial Intelligence, and Operations Research*, edited by L.-M. Rousseau and K. Stergiou (Springer International Publishing, Cham, 2019), p. 163.

[39] J. Marshall, V. Martin-Mayor, and I. Hen, Phys. Rev. A **94**, 012320 (2016).

[40] W. Wang, S. Mandrà, and H. G. Katzgraber, Phys. Rev. E **96**, 023312 (2017).

[41] F. Hamze, D. C. Jacob, A. J. Ochoa, D. Perera, W. Wang, and H. G. Katzgraber, Phys. Rev. E **97**, 043303 (2018).

[42] F. Hamze, J. Raymond, C. A. Pattison, K. Biswas, and H. G. Katzgraber (2019), (arXiv/cond-mat:1906.00275).

[43] I. Hen (2019), (arxiv:quant-ph/1903.10928).

[44] N. N. Schraudolph and D. Kamenetsky, in *Adv. Neural Inf. Process. Syst. 21*, edited by D. Koller, D. Schuurmans, Y. Bengio,

and L. Bottou (Curran Associates, Inc., 2009), p. 1417.

[45] A. Galluccio, M. Loebl, and J. Vondrák, Math. Program. **90**, 273 (2001).

[46] A. Galluccio, M. Loebl, and J. Vondrak, Phys. Rev. Lett. **84**, 5924 (2000).

[47] L. Saul and M. Kardar, Nucl. Phys. B **432**, 641 (1994).

[48] G. Toulouse, Commun. Phys. **2**, 115 (1977).

[49] We note that any gauge transformations suggested above will not change the overall concentration of frustrated plaquettes nor hide the fact that all plaquettes of one sublattice are frustrated.

[50] E. D. Demaine and M. L. Demaine, Graphs and Combinatorics **23**, 195 (2007).

[51] F. R. Kschischang, B. J. Frey, and H.-A. Loeliger, IEEE Transactions on information theory **47**, 498 (2001).

[52] A. Okabe, B. Boots, K. Sugihara, and S. N. Chiu, *Spatial Tessallations — Concepts and Applications of Voronoi Diagrams* (Wiley, New York, 2000).

[53] L. Y. Barash, M. Weigel, M. Borovský, W. Janke, and L. N. Shchur, Comp. Phys. Comm. **220**, 341 (2017).

[54] A. Barzegar, C. Pattison, W. Wang, and H. G. Katzgraber, Phys. Rev. E **98**, 053308 (2018).

[55] Note, however, that to the extent that the chosen population sizes are found to be too small for some of the hardest samples, up to statistical fluctuations the resulting estimates of ρ_s should be considered lower bounds to the actual values of ρ_s.

[56] S. V. Isakov, I. N. Zintchenko, T. F. Rønnow, and M. Troyer, Comput. Phys. Commun. **192**, 265 (2015), (see also ancillary material to arxiv:cond-mat/1401.1084).

[57] T. F. Rønnow, Z. Wang, J. Job, S. Boixo, S. V. Isakov, D. Wecker, J. M. Martinis, D. A. Lidar, and M. Troyer, Science **345**, 420 (2014).

[58] S. Boixo, T. F. Rønnow, S. V. Isakov, Z. Wang, D. Wecker, D. A. Lidar, J. M. Martinis, and M. Troyer, Nat. Phys. **10**, 218 (2014).

[59] V. Privman, ed., *Finite Size Scaling and Numerical Simulation of Statistical Systems* (World Scientific, Singapore, 1990).

[60] J. Houdayer and A. K. Hartmann, Phys. Rev. B **70**, 014418 (2004).

[61] H. G. Katzgraber, M. Körner, and A. P. Young, Phys. Rev. B **73**, 224432 (2006).

[62] B. M. McCoy and T. T. Wu, *The two-dimensional Ising model* (Harvard University Press, Massachusetts, 1973).

[63] R. H. Swendsen and J.-S. Wang, Phys. Rev. Lett. **58**, 86 (1987).

[64] U. Wolff, Phys. Rev. Lett. **62**, 361 (1989).

[65] B. Bollobás, C. Borgs, J. T. Chayes, J. H. Kim, and D. B. Wilson, Random Struct. Algorithms **18**, 201 (2001).

[66] A. Möbius and U. K. Rössler, Phys. Rev. B **79**, 174206 (2009).

[67] We note that while on general grounds we should expect $\kappa = \nu = 1$ for the two-dimensional Ising symmetry considered here, the observed significant deviation from this expectation is an indicator of the strength of scaling corrections present here.

[68] S. Kobe and T. Klotz, Phys. Rev. E **52**, 5660 (1995).

[69] R. Miyazaki, J. Phys. Soc. Jpn. **82**, 1 (2013).